DEEP LEARNING BASED METHOD FOR DENOISING AND IMAGE ENHANCEMENT IN LOW-FIELD MRI

Dang Bich Thuy Le, Meredith Sadinski, Aleksandar Nacev, Ram Narayanan, Dinesh Kumar

Promaxo

ABSTRACT

Deep learning has proven successful in a variety of medical image processing applications, including denoising and removing artifacts. This is of particular interest for low-field Magnetic Resonance Imaging (MRI), which is promising for its affordability, compact footprint, and reduced shielding requirements, but inherently suffers from low signal-to-noise ratio. In this work, we propose a method of simulating scanner-specific images from publicly available, 1.5T and 3T database of MR images, using a signal encoding matrix incorporating explicitly modeled imaging gradients and fields. We apply a stacked, U-Net architecture to reduce noise from the system and remove artifacts due to the inhomogeneous B_0 field, nonlinear gradients, undersampling of k-space and image reconstruction to enhance low-field MR images. The final network is applied as a post-processing step following image reconstruction to phantom images acquired on a 60-67mT MR scanner and demonstrates promising qualitative and quantitative improvements to overall image quality.

***Index Terms*—** MRI, U-Net, deep learning, image enhancement, denoising.

1. INTRODUCTION

For MRI systems, maximizing the signal-to-noise ratio (SNR) is critical for obtaining high quality images. Noise generated during image acquisition will negatively affect image quality, degrade the diagnostic efficacy and accuracy of navigation in MRI-guided procedures, and limit reliability of subsequent imaging tasks such as registration, segmentation, and classification [1]. Low-field MRI systems (less than 1T) inherently have lower SNR than high-field (1.5T - 3T) MRI scanners as SNR increases quadratically or linearly with B_0, depending on whether object noise or electronic noise is dominant [2]. Noise in high-field MRI scanners is typically dominated by the object being imaged, with additional noise from hardware. At low-fields, object noise is negligible and overall noise is dominated by hardware components such as RF coils and spectrometers. This noise has been observed to be Gaussian distributed in the signal domain.

Many deep learning and non-learning based methods to remove noise in MR images have been reported. Balafar [3] has reviewed some widely-used, non-learning methods such as linear Gaussian and Wiener filters, which are simple to implement but image details and edges may be degraded. Markov random field based methods robustly denoise and preserve fine detail but are computationally expensive. Iterative reconstruction algorithms with noise-penalizing regularization have also been used to denoise image data during the reconstruction process [4]. Recently, deep learning based methods have demonstrated the potential for denoising, often outperforming conventional methods. The performance of denoising tasks in conventional methods strongly depends on the estimated noise level [1], while this is not necessarily true in learning based methods. Dongsheng Jiang et al. [1] proposed a 3D, multi-channel, deep convolutional neural network (CNN), using residual learning on high-field brain images with added noise. He compared the performance of models trained on data with added noise of a specific level and, separately, data with added noise of varying levels. He reported that the model trained without a specific noise level showed superior performance compared to either noise-specific level model or other conventional methods. Manjón et al. [5] suggested a two-stage, denoising approach that combined deep learning and conventional, non-local image processing methods. He used the pre-filtered image acquired by an overcomplete patch-based 3D CNN in the first stage as the guide image for a rotational invariant non-local means filter in the second stage to denoise the original image.

In addition to noise, low spatial resolution may limit image quality and interpretability. SNR constraints of low-field scanners make imaging at high resolution difficult. To acquire an image at low-field with the same resolution as one at high-field, while maintaining the same SNR, the number of averages needs to be increased, resulting in an increased acquisition time [6]. According to Marques [6], for a T1-weighted brain image with 1.2 mm isotropic resolution, reducing the magnetic field from 1.5T to 0.5T would require an increase in acquisition time from 9 to 91 minutes, assuming linear dependence of the SNR and the same pulse sequence. Thus, spatial resolution must likely be sacrificed, and post-processing techniques to enhance high-frequency structures, such as edges, of an image are therefore useful. Similar techniques are being used in high-field images to enhance image quality [7, 8, 9].

A challenge in many post-processing techniques, including the deep learning field, is the need for paired, training data. This is burdensome for low-field scanners as public databases contain mostly high-field images. Low-field image data is not widely available. To effectively deploy a deep learning based model on Promaxo reconstructed images, it is important to generate training data that mimics the system in terms of noise and resolution characteristics. Simulated images are an alternative approach and necessary so that the training images are closer to the actual image acquired from the Promaxo scanner.

In this paper, we propose an image enhancement method as a post-processing step for image reconstruction. To train the enhancement network, we also propose a data processing pipeline to generate simulated images from high-field images that incorporates k-space sampling patterns, gradient maps, and B_0 field maps of Promaxo's low-field MRI system. This pipeline is designed to mimic artifacts produced by undersampling, field inhomogeneities, and gradient nonlinearities for the subject device. Images generated from this pipeline are then used to train two different image enhancing networks, which will later be cascaded in the clinical use case scenario. Using a U-Net architecture, the first network is aimed at reducing typical MR image noise, and the second network is aimed at reducing the above-mentioned artifacts.

2. METHOD

2.1. Promaxo Reconstruction Pipeline and Forward Operator

The Promaxo MRI scanner operates at low, non-uniform B_0 field (60-67 mT) over the imaging field of view with nonlinear x- and y-axis electromagnetic gradients and a permanent, built-in z-gradient. The standard image reconstruction pipeline and the proposed implementation of two cascaded trained models to enhance image quality are shown in Fig. 1.

Image reconstruction on the Promaxo MRI system uses a non-Fourier encoding matrix-based linear system that models for nonlinearities in the system, using the formulation

$$S = Em \tag{1}$$

where S is the observed signal, E is the encoding matrix, and m is the image that is solved for. The encoding matrix models the entire system – B_0 field maps, gradient maps, phases induced by the pulse sequence, and coil maps.

The system has multiple receive coils, each making measurements simultaneously. Individual images from each coil are reconstructed initially before being combined into a final image. We call each phase encode within the pulse sequence a single state in the system. For each state, a signal array is measured of length $\mathbf{n}_m$, the length of a single echo acquisition.

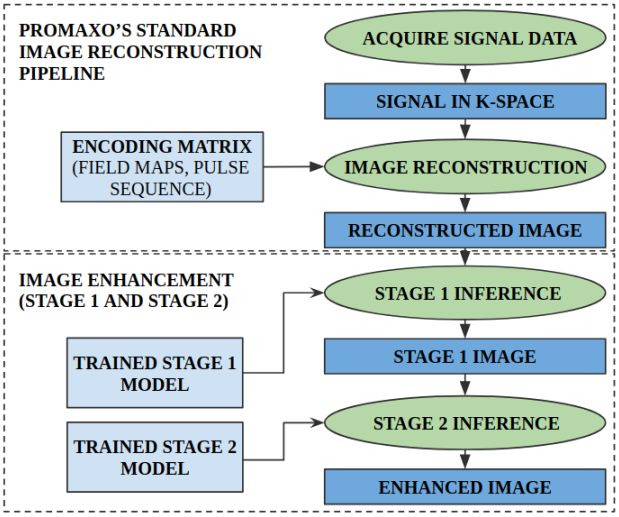

Fig. 1: Overall image reconstruction pipeline of Promaxo. Top: standard image reconstruction pipeline from acquired signal data to reconstructed image using formulation S = Em. Bottom: image enhancement using the two cascaded trained U-Net models which are proposed in this work.

An element of the encoding matrix E for state k and time index i within the readout window can be written as follows:

$$E(p,q) = C^{+}(q)C^{-}(q)exp(j\gamma(A(k,0,i)t_i + B(k,0)G_x + A(k,1,i)t_i + B(k,1)G_y) + j(\gamma B_0 - F(k))t_i) \tag{2}$$

Where $p = k \times n_m + i$ is the index of flattened signal data vector, q is the voxel index, ranging from 0 to length of image vector m, γ is gyromagnetic ratio, and t_i corresponds to the time within the echo window array at index i. The expression above calculates the phase from the gradient profile matrix A (which is the normalized shape of the readout gradient applied for each pulse sequence state), and the phase matrix B (which contains the phase encoding stored for each of x, y and z directions), incorporating the non-uniform field B_0, and the excitation frequency offset matrix F (expressed in radians). Matrix $\mathbf{C}^{-}$ models the receive coil sensitivity map in terms of amplitude and phase of each voxel in the image. Matrix $\mathbf{C}^{+}$ models the transmit coil sensitivity map. G_x and G_y specifies field maps measured from x and y gradients respectively.

We use formulation 1 to generate observed signal by applying this encoding matrix as a transformation, which will be referred to as the forward operator, on a ground truth image. We start with the ground truth image and pass it through the forward operator to generate signal data. The generated signal resembles typical signal data from the Promaxo MRI system.

2.2. Training and Testing Dataset

Paired sets of images used for training were generated from public MR images from the Cancer Imaging Archive [7].

We used 5 datasets (PROSTATEx [10], Prostate-3T [11], Prostate Fused-MRI-Pathology [12], Prostate-diagnosis [13], and Prostate-MRI [14]), containing T1, T2, proton density, diffusion weighted, and dynamic contrast enhanced images from 1.5T or 3T scanners.

The stage 1 network was trained on two types of training data: (1) training data generated by adding noise in k-space (Noise model A, Fig. 2), and (2) training data with noise added in the image domain (Noise model B, Fig. 2). Noise consisted of varying levels of additive white Gaussian noise.

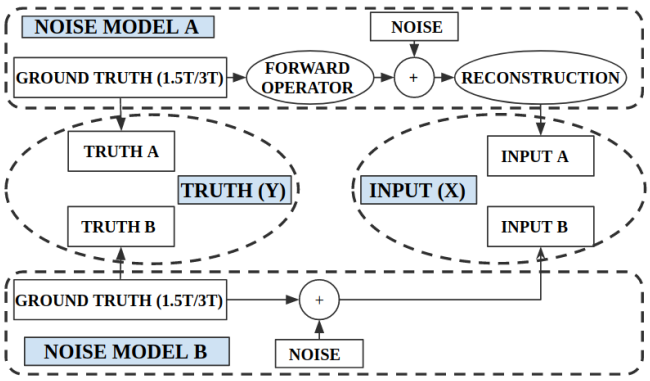

Fig. 2: Training data generation for stage 1 network. Top: Noise model A in which training data is constructed by adding noise in k-space. Bottom: Noise model B in which training data is constructed by adding noise in the image domain. Middle: training pool of stage 1 network, including truth and input from noise model A and B.

The stage 2 network was trained on images that contain artifacts characteristic of the Promaxo MRI system and commonly observed in other systems with main field inhomogeneities, non-linear gradients, and sub-Nyquist k-space undersampling. T1- and T2-weighted, axial series acquired without an endorectal coil were extracted from the above-mentioned data pool to be processed for training input into the stage 2 network. Two datasets were used: PROSTATEx (429 image series extracted) and Prostate-3T (57 image series extracted). Construction of training data for the stage 2 network is shown in Fig. 3 below.

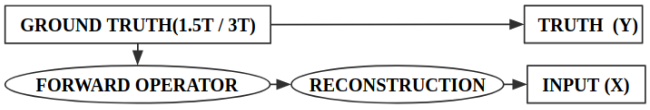

Fig. 3: Data generation for stage 2 using forward operator.

2.3. Network

A U-Net architecture was chosen for both stage 1 and 2 networks. We used the modified version of the Ronneberger U-Net approach [15]. For the stage 2 network, we investigated two networks: (1) a network with one U-Net layer and (2) a network with two U-Net layers in order to better approximate the target function with increased nonlinearity and get better feature representations by increasing depth [16]. We did not investigate using more than two U-Net layers due to the increasing difficulty of network optimization and increased risk of overfitting with additional network complexity.

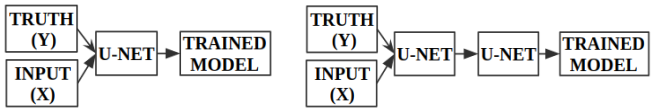

(a) One U-Net layer network (b) Two U-Net layer network

Fig. 4: Layout of stage 2 network using 1 or 2 U-Net layers.

We used a combination of mean squared error (L_{MSE}) and perceptual loss functions (L_{VGG}) as the loss function for the network as

$$L = L_{MSE} + \lambda L_{VGG} \tag{3}$$

Optimizing for L_{MSE} alone may result in loss of details, especially high-frequency details. Perceptual loss functions such as pre-trained loss on VGG-19 network [17] helps to reduce over smoothing often seen for purely MSE-based loss functions. We used RMSprop to minimize loss. Initial learning rate was set to 0.001.

3. RESULTS

For stage 1, aimed at removing noise, we trained two models: one with training data with noise model A (Fig. 2), referred as Model 1.1, and another with training data with both noise model A and B (Fig. 2), referred as Model 1.2. For stage 2, aimed at reducing artifacts, we trained two models: one with only one U-Net layer (Fig. 4a), referred as Model 2.1 and another with two U-Net layers (Fig. 4b), referred as Model 2.2. We evaluated the performance of these models using three quantitative metrics: normalized root mean squared error (NRMSE), peak signal to noise ratio (PSNR), and structural similarity (SSIM).

Model 1.2 (noise added in both signal and image domain) performs better than Model 1.1 (noise added in signal domain only), and Model 2.2 (two U-Net layers) performs better than Model 2.1 (one U-Net layer) because predicted images from these models have lower NRMSEs, higher PSNRs, and higher SSIMs values.

Table 1: Evaluation metrics of network performance for the stage 1 (left) and stage 2 (right) networks separately. Values which indicate better performance are shown in bold.

	Model 1.1	**Model 1.2**
NRMSE	0.383	**0.262**
PSNR	20.8	**24.1**
SSIM	0.409	**0.512**

	Model 2.1	**Model 2.2**
NRMSE	0.401	**0.372**
PSNR	26.4	**27.0**
SSIM	0.342	**0.372**

To validate each stage independently, as well as the concatenation of stages 1 and 2, we used 33, T1- and T2-weighted, axial, 3D image series consisting of a total of 960 2D image slices from Prostate MR Image Database [18]. This data did not participate in any prior training, testing, or validation steps of the individual stage 1 or stage 2 networks. Simulated Promaxo images were generated from these high-field series using the noise model A described in Fig. 2. These simulated Promaxo images in conjunction with their ground truth are used as input images for this validation study. Table 2 shows the results of this validation study. The two-stage cascaded implementation outperforms both the stage 1 and 2 independent implementations.

Table 2: Performance metrics for an independent test set of 960, 2D slices from 11 T1- and T2-weighted image series. Values which indicate better performance are shown in bold.

	No model	**Stage 1 only**	**Stage 2 only**	**Both stage 1 & 2**
NRMSE	0.712	0.669	0.652	**0.633**
PSNR	30.091	30.636	30.857	**31.112**
SSIM	0.557	0.587	0.586	**0.590**

Fig. 5 shows a representative example from the testing dataset. The forward operator is applied to the ground truth 3T image (left) generating the simulated, low-field image (middle) which is then processed with the cascaded, stage 1 and stage 2 models (right).

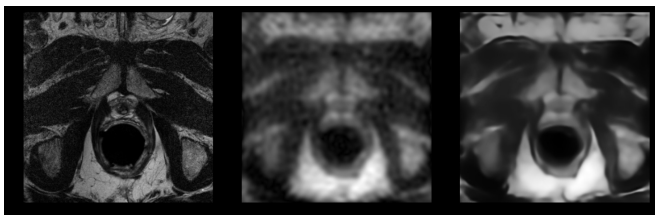

Fig. 5: Deploying the two stage cascaded models on a simulated, low-field image generated from a 3T image. Left: 3T image (ground truth). Middle: simulated image generated using the forward operator (input). Right: simulated image after being processed with two stage cascaded models.

Low-field phantom images acquired with the Promaxo scanner before and after image enhancement with various models are shown in figures 6 and 7. Two phantoms are shown: the small extremity ACR phantom (Fig. 6) and a phantom made in-house consisting of tubes filled with different contrast media with different MR properties (Fig. 7). The tubes are placed in a cylindrical holder and the contrast media are filtered water, CuSO4 solution, commercial mineral oil, olive oil, silicone oil, GdCl solution, and industrial mineral oil. Since the stage 2 network was trained without noise added, while noise in the real world images always exists, we do not implement the stage 2 network alone to our acquired images. Both the stage 1 model alone and combination of stage 1 and stage 2 models show less noise and improve conspicuity of structures. The proposed methods denoised and enhanced image quality most accurately as shown in the enlarged images in figures 6 and 7. These results are consistent with the quantitative comparison in table 1 and 2.

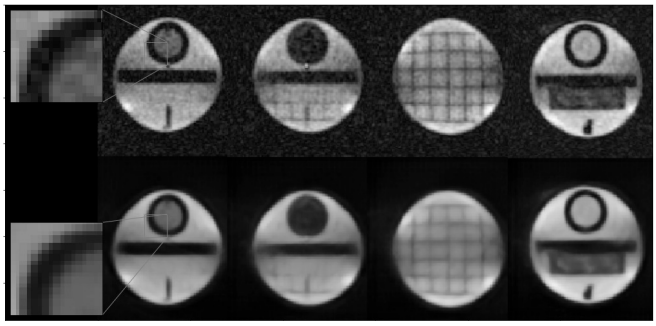

Fig. 6: Low-field phantom images acquired on the Promaxo scanner with and without deploying stage 1 denoising model. Top: noisy image. Bottom: image going through the stage 1 denoising model. Enlarged views are shown to the left.

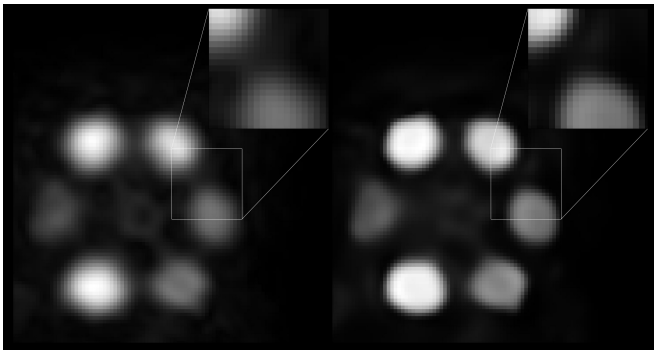

Fig. 7: Low-field images from Promaxo's scanner. Left: noisy image. Right: image going through the two stage cascaded models. Enlarged views are shown in upper right of each image.

4. CONCLUSION

In this paper, we present an approach to generate training data from high-field MRI images that mimics the non-uniform, non-linear gradient fields of Promaxo's low-field MRI system. We used a U-Net architecture to train a two-stage denoising and image enhancing approach. We have shown that following iterative reconstruction, low-field Promaxo image data processed with these trained models demonstrates improvements in fine structure visualization. Concordantly, PSNR, SSIM and NRMSE show quantitative improvement in image quality following inference with trained models on simulated Promaxo data. In the future, this training approach could be extended to model additional specific types of noise and artifacts, and thus facilitate a better deep learning network to detect and eliminate them to improve image fidelity.

5. REFERENCES

[1] Dongsheng Jiang, Weiqiang Dou, Luc Vosters, Xiayu Xu, Yue Sun, and Tao Tan, "Denoising of 3D magnetic resonance images with multi-channel residual learning of convolutional neural network," *Japanese journal of radiology*, vol. 36, no. 9, pp. 566–574, 2018.

[2] Dwight George Nishimura, *Principles of magnetic resonance imaging*, Stanford University, 1996.

[3] MA Balafar, "Review of noise reducing algorithms for brain MRI images," *methods*, vol. 10, pp. 11, 2012.

[4] Michael Lustig, David Donoho, and John M Pauly, "Sparse MRI: The application of compressed sensing for rapid MR imaging," *Magnetic Resonance in Medicine: An Official Journal of the International Society for Magnetic Resonance in Medicine*, vol. 58, no. 6, pp. 1182–1195, 2007.

[5] José V Manjón and Pierrick Coupé, "MRI denoising using deep learning," in *International Workshop on Patch-based Techniques in Medical Imaging*. Springer, 2018, pp. 12–19.

[6] José P Marques, Frank FJ Simonis, and Andrew G Webb, "Low-field MRI: An MR physics perspective," *Journal of magnetic resonance imaging*, vol. 49, no. 6, pp. 1528–1542, 2019.

[7] Pejman Rasti, Morteza Daneshmand, Fatih Alisinanoglu, Cagri Ozcinar, and Gholamreza Anbarjafari, "Medical image illumination enhancement and sharpening by using stationary wavelet transform," in *2016 24th Signal Processing and Communication Application Conference (siu)*. IEEE, 2016, pp. 153–156.

[8] Xu Yan, Min-Xiong Zhou, Ling Xu, Wei Liu, and Guang Yang, "Noise Removal of MRI Data with Edge Enhancing," in *2011 5th International Conference on Bioinformatics and Biomedical Engineering*. IEEE, 2011, pp. 1–4.

[9] Hong Zheng, Kun Zeng, Di Guo, Jiaxi Ying, Yu Yang, Xi Peng, Feng Huang, Zhong Chen, and Xiaobo Qu, "Multi-contrast brain MRI image super-resolution with gradient-guided edge enhancement," *IEEE Access*, vol. 6, pp. 57856–57867, 2018.

[10] L Geert, D Oscar, B Jelle, K Nico, and H Henkjan, "Prostatex challenge data. The Cancer Imaging Archive," 2017.

[11] G Litjens, J Futterer, and H Huisman, "Data from prostate-3t: The Cancer Imaging Archive," 2015.

[12] Anant Madabhushi and Michael Feldman, "Fused Radiology-Pathology Prostate Dataset," *The Cancer Imaging Archive. Available online: http://doi. org/10.7937 K*, vol. 9, 2016.

[13] B Nicolas Bloch, Ashali Jain, and C Carl Jaffe, "Data from PROSTATE-DIAGNOSIS. The Cancer Imaging Archive," Tech. Rep., accessed 1/18/18, 10.7937, 2015.

[14] P Choyke, B Turkbey, P Pinto, et al., "Data From PROSTATE-MRI," *The Cancer Imaging Archive. Available online: http://doi. org/10.7937 K*, vol. 9, 2016.

[15] Olaf Ronneberger, Philipp Fischer, and Thomas Brox, "U-net: Convolutional networks for biomedical image segmentation," in *International Conference on Medical image computing and computer-assisted intervention*. Springer, 2015, pp. 234–241.

[16] Jiuxiang Gu, Zhenhua Wang, Jason Kuen, Lianyang Ma, Amir Shahroudy, Bing Shuai, Ting Liu, Xingxing Wang, Gang Wang, Jianfei Cai, et al., "Recent advances in convolutional neural networks," *Pattern Recognition*, vol. 77, pp. 354–377, 2018.

[17] Karen Simonyan and Andrew Zisserman, "Very deep convolutional networks for large-scale image recognition," *arXiv preprint arXiv:1409.1556*, 2014.

[18] "Prostate MR Image Database," http://prostatemrimagedatabase.com.